

Wigner–Husimi phase-space structure of quasi-exactly solvable sextic potential

Angelina N. Mendoza Tavera^{1†}, Adrian M. Escobar Ruiz^{1†},
Robin P. Sagar^{2††}

¹Departamento de Física, Universidad Autónoma Metropolitana - Iztapalapa, Rafael Atlixco 186, CDMX, 09340, Ciudad de México, México.

²Departamento de Química, Universidad Autónoma Metropolitana - Iztapalapa, Rafael Atlixco 186, CDMX, 09340, Ciudad de México, México.

Contributing authors: cbi2182800711@xanum.uam.mx;
admau@xanum.uam.mx; sagar@xanum.uam.mx;

†These authors contributed equally to this work.

Abstract

In this study, we compare the Wigner function \mathbf{W} , its modulus, and the Husimi distribution \mathbf{H} in a one-dimensional quantum system exhibiting a transition from a single-well to a double-well configuration, using the quasi-exactly solvable sextic oscillator as a representative example. High-accuracy variational wavefunctions for the lowest states are used to compute two-dimensional phase-space structures, one-dimensional marginals, and the corresponding Shannon entropies, mutual information, and Cumulative Residual Jeffreys divergences. The analysis shows that the Wigner representation is uniquely responsive to interference effects and displays clear, nonmonotonic entropic behavior as the wells separate, whereas the modulus-Wigner and Husimi distributions account only for geometric splitting or coarse-grained delocalization. These findings establish a quantitative hierarchy in the ability of \mathbf{W} , $|\mathbf{W}|$, and \mathbf{H} to resolve structural changes in a quantum state and provide a general framework for assessing the descriptive power of different phase-space representations in systems with emerging bimodality or tunneling.

1 Introduction

Phase-space formulations of quantum mechanics provide a unified framework for analyzing coherence, interference, and localization through quasiprobability distributions such as the Wigner and Husimi functions. Since the original works of Wigner [1] and Husimi [2], these representations have become indispensable in quantum optics, semiclassical dynamics, and information theory. Their versatility has been demonstrated in AMO physics, including coherence in Talbot–Lau interferometry [3], optical quantum communication via stochastic and Wigner formalisms [4], and phase-space analyses of instabilities in Rydberg complexes [5]. Broader developments—such as generalized Wigner families for finite-level systems [6] and conceptual studies highlighting the atom as a central building block of modern physics [7]—further underscore the importance of phase-space methods.

The Wigner function encodes the full quantum structure of a state, including its regions of negativity associated with nonclassical interference [8], whereas the Husimi distribution provides a positive-definite, Gaussian-smeared semiclassical portrait [9–11]. Related approaches such as the Wigner–Kirkwood expansion [12] incorporate systematic semiclassical corrections. Recently, the modulus $|W|$ has attracted renewed interest as an intermediate representation preserving geometric phase-space features while eliminating sign oscillations [13]. Applications include the study of coherence and classical inhomogeneities [14] and nonlinear atom–light interactions [15].

Beyond structural aspects, these phase-space distributions admit a rich information-theoretic characterization through Shannon, Rényi, Tsallis, and Fisher entropies, as well as correlation measures. Shannon entropies quantify global delocalization [16], while the entropic uncertainty relation provides a sharper bound than the variance-based Heisenberg relation [17]. These concepts have been applied from AMO to condensed-matter physics [18–21], including complexity [21], quantum-phase transitions [10], and entanglement studies [11]. Tsallis entropies further illuminate electron correlation and nonlinear structure [22, 23].

A broad set of measures also exists for quantifying statistical correlations. These include correlation coefficients [24, 25], mutual information in position and momentum spaces [26, 27], and higher-order interaction information [28–30]. Such tools have been applied to nuclear systems [31], Bose–Einstein condensates [32–34], chemical reactivity [35], and wave-packet dynamics [36]. Their relevance to AMO-related phase-space analysis is reflected in recent Wigner and Husimi studies [3, 12, 14].

Despite these developments, a unified comparative study of the Wigner, $|W|$, and Husimi quasiprobabilities within a single, continuously tunable quantum system—using modern information-theoretic indicators—has been missing. While Wigner and Husimi functions have been widely applied, no previous work has systematically compared them, together with $|W|$, across their two-dimensional structure, marginals, entropies, mutual information, and CRJ divergences. A natural setting for such an investigation is the quasi-exactly solvable (QES) sextic potential, which admits analytic eigenstates for part of its spectrum and interpolates smoothly between single- and double-well regimes. Its algebraic foundations were developed in the pioneering works [37–39] and later linked to orthogonal-polynomial structures [40]. Recent SUSY and WKB developments further confirm its role as a benchmark model [41, 42].

Our recent study [43] showed that one-dimensional densities $|\psi(x)|^2$ and $|\phi(p)|^2$ already reveal tunneling, quasi-degeneracy, and parity effects through entropic and divergence-based indicators. However, that analysis remained strictly in configuration and momentum space and did *not* construct any phase-space distributions nor examine Wigner negativity or smoothing effects.

In this work, we extend the informational analysis of [43] to the *full phase-space domain*, providing the first unified comparison of the Wigner function $W(x, p)$, its modulus $|W(x, p)|$, and the Husimi distribution $H(x, p)$ for the QES sextic oscillator. To our knowledge, no prior study has jointly compared (i) Wigner, (ii) modulus-Wigner, and (iii) Husimi representations across: (a) their full phase-space structure, (b) their marginals, (c) their entropies, (d) their mutual information, and (e) their CRJ divergences—features inaccessible to purely one-dimensional approaches.

The central question guiding this work is: *How do $W(x, p)$, $|W(x, p)|$, and $H(x, p)$ differ in their structural and information-theoretic response to the single- to double-well transition in the QES sextic potential?*

The paper is organized as follows. Section 2 introduces the QES sextic potential and summarizes the variational construction of low-lying states. Section 3 reviews the three quasiprobability representations. Section 4 presents the main phase-space results. Section 5 discusses entropic and correlation measures derived from the marginals, while Section 6 incorporates mutual information and CRJ divergences. Section 7 summarizes the main insights, and Section 8 outlines possible directions for future work. Appendices A and B provide supporting algebraic and numerical details.

2 The model: QES sextic potential

Quasi-exactly solvable (QES) models form a distinguished class of quantum systems in which a finite portion of the spectrum can be determined in closed algebraic form, while higher states require approximation. This intermediate status between exactly solvable and generic models makes them particularly valuable: algebraic eigenstates provide exact benchmarks, whereas the non-algebraic sector tests the reliability of variational, numerical, and information-theoretic methods. The sextic QES potential is particularly rich, as tuning its control parameter λ drives the system from a single-well regime into a symmetric double well, giving rise to localization-delocalization transitions, quasi-degenerate tunneling doublets, and nonperturbative instanton effects. These features render QES systems natural testbeds for studying the interplay between algebraic solvability, semiclassical physics, and entropic measures of coherence and correlation.

So, we focus on the one-dimensional spectral problem of non-relativistic quantum mechanics,

$$\mathcal{H}\psi(x) = E\psi(x), \quad \psi(x) \in \mathcal{L}^2(\mathbb{R}), \quad (1)$$

defined on the full real line $x \in (-\infty, \infty)$. The Hamiltonian operator is of the form

$$\mathcal{H} = -\frac{\hbar^2}{2m} \frac{d^2}{dx^2} + V^{\text{QES}}(x; \lambda), \quad (2)$$

with particle mass m and the quasi-exactly solvable sextic potential

$$V^{\text{QES}}(x; \lambda) = \frac{1}{2} \left(x^6 + 2x^4 - 2(2\lambda + 1)x^2 \right), \quad (3)$$

where $\lambda \in \mathbb{R}$ is the control parameter.

This potential belongs to the class of quasi-exactly solvable (QES) models: for special values of λ , a finite subset of eigenstates can be obtained in closed algebraic form, while the remainder requires approximation. Hereafter we adopt atomic units, $\hbar = 1$ and $m = 1$. Equation (1) with potential (3) defines the central problem addressed in this work.

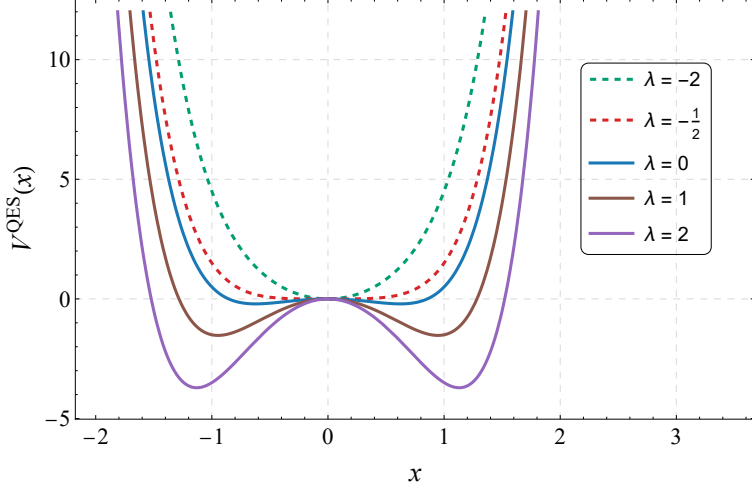


Fig. 1: QES confining sextic potential $V^{\text{QES}}(x; \lambda)$ in (3) for different values of the parameter λ . For $\lambda > -\frac{1}{2}$ it develops two symmetric degenerate minima, and the λ -independent maximum located at $x = 0$ corresponds to a potential energy $V = 0$.

2.1 Variational calculations of low-lying states

To solve the spectral problem (2), we employ a variational approach. For the explicit calculations, we follow the methodology presented in [43]. Since the full construction of the variational ansatz and the details and results of its optimization are thoroughly discussed in that reference, we do not reproduce them here, and instead summarize only the essential elements relevant for the present work. Details on the convergence and accuracy of calculation are presented in Appendix B.

The real trial wavefunction for the n th state is chosen in the form

$$\psi_n^{(\text{var})}(x; \lambda) = Q_k^{(n)}(x; \lambda) e^{-x^4/4}, \quad n = 0, 1, 2, \dots, \quad (4)$$

where the exponential factor guarantees the correct asymptotic decay as $|x| \rightarrow \infty$, and the polynomial $Q_k^{(n)}(x; \lambda)$ enforces the exact parity symmetry of the Hamiltonian under the reflection $x \rightarrow -x$.

Explicitly, for the ground state ($n = 0$), the polynomial factor

$$Q_k^{(0)}(x; \lambda) = \sum_{i=0}^k c_i x^{2i} , \quad (5)$$

is of degree $k = k(n)$ in the variable x^2 . Thus $Q_k^{(0)}(x) = Q_k^{(0)}(-x)$, and it has no real zeros. The linear coefficients c_i are determined by minimizing the variational energy,

$$E^{(\text{var})} = \frac{\int_{-\infty}^{\infty} \psi_n^{(\text{var})} \hat{H} \psi_n^{(\text{var})} dx}{\int_{-\infty}^{\infty} (\psi_n^{(\text{var})})^2 dx} ; \quad \frac{\partial E^{(\text{var})}}{\partial c_i} = 0 , \quad i = 1, 2, \dots, k . \quad (6)$$

The first excited state $n = 1$ is, instead, described by an odd polynomial factor $Q_k^{(1)}(x; \lambda)$, which possesses a single real root at $x = 0$, as required by parity.

For excited states ($n > 0$), several coefficients in the polynomials $Q_k^{(n)}(x; \lambda)$ can be fixed by enforcing orthogonality and normalization

$$\langle \psi_n | \psi_{\tilde{n}} \rangle = \delta_{n, \tilde{n}} , \quad (7)$$

while the remaining parameters are optimized by minimizing the corresponding energy expectation value. The polynomial order $k = k(n)$ is chosen minimally to ensure that the resulting variational energies reach a relative accuracy of $\sim 10^{-8}$ when compared to Lagrange-mesh [44] calculations. This ansatz also admits closed-form Fourier transforms of the wavefunctions, enabling accurate momentum-space and entropy analyses.

That way, the resulting variational energies agree with exact solutions and with Lagrange-mesh results to within relative errors of order 10^{-8} , confirming the reliability of the trial functions across all relevant values of the control parameter λ .

3 Phase-space representations

Phase-space quasiprobability functions provide complementary viewpoints on the structure of a quantum state. In this work, we focus on three widely used representations—the Wigner distribution $W(x, p)$, its (normalized) absolute value $|W(x, p)|$, and the Husimi function $H(x, p)$ —and study their similarities and differences for the low-lying states of the QES sextic oscillator. Although all three originate from the density operator $\hat{\rho} = |\psi\rangle\langle\psi|$, each representation encodes coherence, interference, and smoothing in a distinct manner, making a systematic comparison essential.

3.1 The Wigner function

For a fixed quantum state n of the QES Hamiltonian (2), the corresponding quasiprobability distribution Wigner function $W_n(x, p)$, defined in the phase-space (x, y) , is given by

$$W_n(x, p) = \frac{1}{\pi} \int_{-\infty}^{\infty} \psi_n^*(x + y) \psi_n(x - y) e^{2ipy} dy. \quad (8)$$

It is a real-valued function normalized according to

$$\int_{-\infty}^{\infty} \int_{-\infty}^{\infty} W_n(x, p) dx dp = 1, \quad (9)$$

and its marginals yield the probability quantum densities, namely

$$\int_{-\infty}^{\infty} W_n(x, p) dp = |\psi_n(x)|^2, \quad \int_{-\infty}^{\infty} W_n(x, p) dx = |\phi_n(p)|^2. \quad (10)$$

Despite its normalization properties, $W_n(x, p)$ is not guaranteed to be non-negative. Its negative lobes play an important role: they are widely regarded as signatures of quantum interference, nonclassicality, and phase-space coherence.

In the sextic oscillator studied here, the evolution of these negative regions as the coupling λ varies provides detailed information about the emergence of tunneling, lobe separation, and parity-dependent interference. In this work, we will focus exclusively on the two lowest states, namely the ground state ($n = 0$) and the first excited state ($n = 1$).

3.2 The modulus of the Wigner function

For each eigenstate, we consider the modulus of the Wigner distribution, $|W_n(x, p)|$, as a strictly non-negative phase-space representation. Although it does not correspond to any operator ordering and is therefore not a true quasiprobability in the Weyl–Heisenberg sense, $|W_n|$ has proven useful as an interference–suppressed diagnostic: by removing the sign oscillations responsible for Wigner negativity, it filters out fine interference fringes while preserving the global geometric structure of the state.

Since $|W_n|$ is not normalized, we always use its normalized version when computing entropies or marginals, i.e.,

$$|W_n| \rightarrow \frac{|W_n(x, p)|}{\int_{-\infty}^{\infty} \int_{-\infty}^{\infty} |W_n(x, p)| dx dp}. \quad (11)$$

This ensures a consistent comparison with the normalized Wigner and Husimi distributions.

In practice, $|W_n|$ inherits the main phase-space features of W_n (peak locations, lobe separation, elongation) while eliminating its alternating sign pattern, and remains more structured than the Gaussian–smoothed Husimi function, making it an informative intermediate description.

3.3 The Husimi function

The Husimi function associated with the n th eigenstate is defined as the squared overlap of ψ_n with the minimum-uncertainty coherent states $|x, p\rangle$,

$$H_n(x, p) = \frac{1}{\pi} |\langle x, p | \psi_n \rangle|^2, \quad (12)$$

which is equivalent to a Gaussian smearing of the corresponding Wigner function,

$$H_n(x, p) = \frac{1}{\pi} \int_{-\infty}^{\infty} \int_{-\infty}^{\infty} W_n(x', p') \exp[-(x - x')^2 - (p - p')^2] dx' dp'. \quad (13)$$

The Husimi function H_n is smooth, positive definite, and normalized to unity. Consequently, it lacks the negativity that characterizes W_n , but retains information about the spatial and momentum extent of the state. Its smoothing kernel has unit minimal uncertainty, and therefore washes out rapid oscillations and interference fringes. Comparing H_n with W_n and $|W_n|$ provides a clear picture of which features in the Wigner function are robust under coarse graining and which arise solely from nonclassical oscillatory structure.

3.4 Rationale for systematic comparison

The three quasiprobability functions considered here for each quantum state $n = 0, 1$ represent a hierarchy of differing degrees of coarse graining:

$$W_n \longrightarrow |W_n| \longrightarrow H_n.$$

The Wigner function retains full quantum coherence and interference; $|W_n|$ removes sign information but keeps much of the structural detail; and H_n provides a non-negative, smoothed representation closely connected to semiclassical phase-space descriptions.

A central goal of this work is to quantify how these representations differ as the potential is tuned through single-well and double-well regimes. By analyzing two-dimensional plots, marginals, entropies, mutual information, and Cumulative Residual Jeffreys divergences for W_n , $|W_n|$, and H_n (with $n = 0, 1$), we obtain a unified framework for assessing their descriptive capacities and identifying the distinctive features each one contributes to the analysis of the sextic QES oscillator.

4 2D phase-space structure of low-lying states

Before analyzing the phase-space distributions, we introduce the state-dependent critical couplings $\lambda_c^{(n)}$. For each eigenstate n , $\lambda_c^{(n)}$ denotes the value of λ at which the energy E_n reaches the height of the central maximum of the potential. At this point the state becomes energetically comparable to the barrier top, and tunneling effects begin to appear. These $\lambda_c^{(n)}$ serve as natural reference markers in the phase-space and

information-theoretic analysis that follows. In particular, for the two lowest states we have:

$$\lambda_0 = \lambda_c^{(0)} = 0.7329, \quad \lambda_1 = \lambda_c^{(1)} = 1.4209. \quad (14)$$

Now, the Wigner function, its modulus, and the Husimi distribution provide complementary insights into how the quantum state is organized in phase space. In this section, we analyze the two lowest states ($n = 0, 1$) of the QES sextic potential and examine how their phase-space profiles evolve as the coupling parameter λ drives the system from a shallow single-well configuration to a well-developed double-well potential. Throughout, the emphasis is placed on identifying the characteristic signatures that distinguish W , $|W|$, and H .

It is worth mentioning that one-dimensional systems, such as the QES potential, allow a complete graphical description and analysis of phase-space distributions. In higher dimensions, such an analysis is restricted to projections in order to appreciate the behavior of these distributions.

4.1 Ground state ($n = 0$)

The Figure 2 shows that the Wigner function $W(x, p)$ for $n = 0$ is initially unimodal for small λ , with a single peak centered at $(x, p) = (0, 0)$. As the potential develops a central barrier, the phase-space density elongates along the x -axis and eventually splits into two lobes located near the classical minima of the double well. In this regime, $W(x, p)$ exhibits alternating positive and negative oscillations between the two lobes, reflecting interference between amplitudes localized in opposite wells. In particular, at $\lambda = -\frac{3}{4}$ (single-well regime), $W(x, p)$ exhibits negative regions that are extremely small and not perceptible to the eye, whereas at $\lambda = 4$ (full double-well regime) the negative regions become clearly visible.

The modulus $|W(x, p)|$, removes the sign pattern associated with interference while retaining the geometric structure of the distribution. The region between the two phase-space lobes becomes uniformly positive, and the fine interference ripples present in W are suppressed without eliminating the overall elongation or the separation of the main maxima. The resulting distribution lies midway between the oscillatory Wigner profile and the smoothed Husimi function.

The Husimi distribution $H(x, p)$ presents a markedly different picture: its Gaussian coarse graining smooths out the oscillations entirely and produces a strictly positive phase-space density with broader contours. In the single-well region, H is almost circular near the origin; as λ increases, it bifurcates into two smooth, separated hills that track the underlying potential minima. The suppressed negativity and increased width of H reflect the reduced resolution of coherent-state smoothing and provide a more classical visual representation of the state.

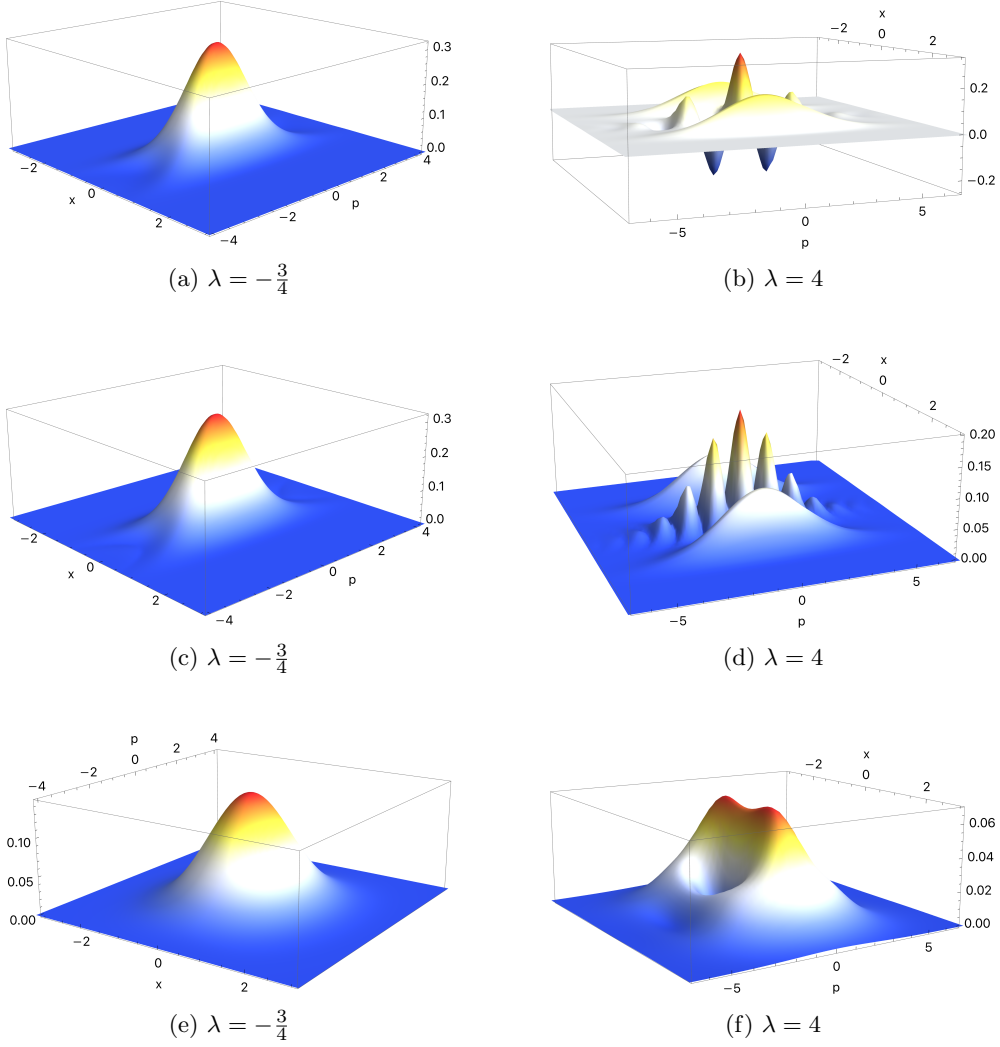


Fig. 2: Wigner quasiprobability distribution $W(x, p)$ (top), modulus of the Wigner function $|W(x, p)|$ (middle), and Husimi distribution $H(x, p)$ (bottom) for the ground state $n = 0$ of the QES sextic oscillator at $\lambda = -\frac{3}{4}$ and $\lambda = 4$.

4.2 First excited state ($n = 1$)

For the first excited state ($n = 1$) shown in Figure 3, the Wigner function displays the characteristic sign change associated with odd parity: a central nodal line at $x = 0$ separates two large lobes of opposite sign. In the single-well regime these lobes are close to each other, producing a compact alternating pattern in (x, p) . As the potential becomes double-welled, the lobes shift outward and become aligned with the classical turning points, while strong interference fringes appear between them. This evolution

is particularly visible in the p -direction, where the oscillatory pattern becomes more structured as the state develops distinct left- and right-localized components. Even at $\lambda = -\frac{3}{4}$ (single-well regime), the Wigner function exhibits pronounced negative regions. This behavior is markedly different from that of the ground state.

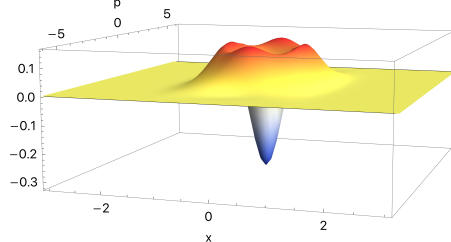
The modulus $|W(x, p)|$ again removes the nodal sign structure, resulting in two equally-weighted positive peaks separated by a ridge of smaller amplitude. The outward motion of these peaks with increasing λ mirrors the movement of the wavefunction nodes in configuration space. Compared with $n = 0$, the excited-state modulus retains more residual fine structure, indicating that $|W|$ still encodes aspects of the interference present in W , even when negativity is removed.

For the Husimi distribution $H(x, p)$, the antisymmetric character of the state is expressed not through negativity (which H cannot display) but through the presence of a broad valley along the $x = 0$ axis. This smooth depletion replaces the sharp nodal line seen in W . Note that the Wigner function retains more of the nodal structure as compared to the Husimi distribution. As λ increases and the two classical wells deepen, the Husimi density separates into two wide, rounded maxima located near the classical minima, each corresponding to a coarse-grained envelope of the left- and right-localized lobes.

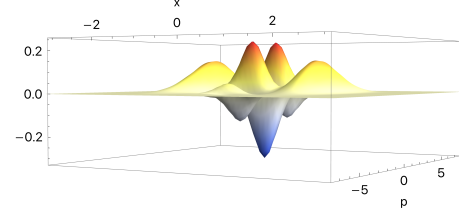
4.3 Comparison and structural trends

As λ increases, the structural differences among W , $|W|$, and H observed in Figs. 2-3 can be summarized as follows:

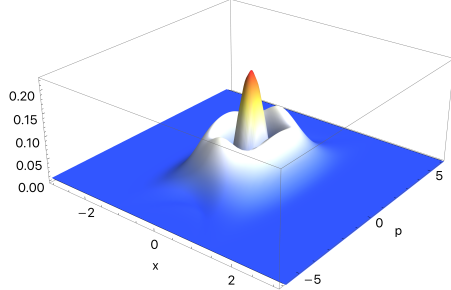
- **Before tunneling ($\lambda \ll \lambda_c$):** For $n = 0$, W , $|W|$, and H are nearly identical (Fig. 2), all showing a single central lobe with minimal negativity, whereas for $n = 1$, these three representations already differ (Fig. 3). In particular, W exhibits opposite-sign lobes separated by a nodal line, $|W|$ retains a two-lobe geometry free of negativity, and H yields a broader, fully positive distribution with a smooth central valley.
- **After tunneling ($\lambda > \lambda_c$):** Both states develop well-separated lobes, and the three representations diverge: W displays interference fringes, $|W|$ retains the two-lobe geometry while eliminating all sign changes, but the interference fringes persist as positive oscillations, and H provides the smoothest, most classical-looking profile (Figs. 2-3).
- **Cross-state comparison:** In the post-tunneling regime, $|W|$ for $n = 0$ and $n = 1$ becomes remarkably similar, as sign removal suppresses parity-induced differences that remain evident in W and, to a lesser degree, in H .
- **Role of parity:** Even states produce a single symmetric lobe in W , while odd states exhibit two opposite-sign lobes separated by a nodal line. Taking the modulus $|W|$ removes negativity but preserves this one-peak (even) versus two-peak (odd) geometry, whereas the Husimi function H smooths the structure into broad semiclassical peaks. These parity-imprinted features determine the distinct behavior of the $n = 0$ and $n = 1$ marginals, especially as λ approaches the tunneling regime.



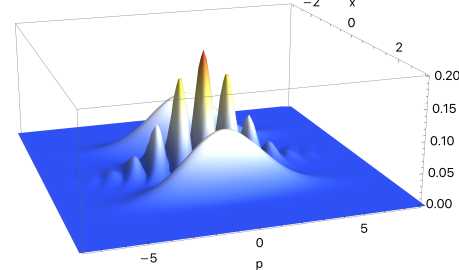
(a) $\lambda = -\frac{3}{4}$



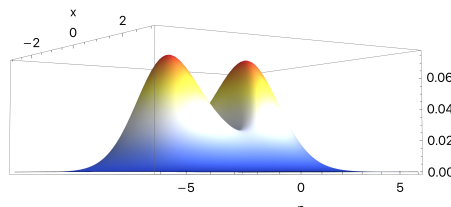
(b) $\lambda = 4$



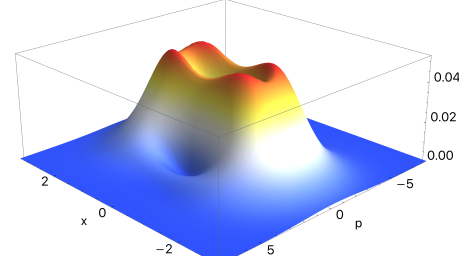
(c) $\lambda = -\frac{3}{4}$



(d) $\lambda = 4$



(e) $\lambda = -\frac{3}{4}$



(f) $\lambda = 4$

Fig. 3: Wigner quasiprobability distribution $W(x, p)$ (top), modulus of the Wigner function $|W(x, p)|$ (middle), and Husimi distribution $H(x, p)$ (bottom) for the first excited state $n = 1$ of the QES sextic oscillator at $\lambda = -\frac{3}{4}$ and $\lambda = 4$.

The phase-space plots above reveal the full two-dimensional structure of W , $|W|$, and H . We now turn to their position- and momentum-space marginals, which capture the projections of this structure onto the physical axes and serve as the fundamental inputs for the entropy, mutual-information, and CRJ analyses that follow.

5 1D phase-space structure of low-lying states: marginal distributions

The position and momentum marginals derived from $W(x, p)$, $|W(x, p)|$, and $H(x, p)$ provide simplified one-dimensional projections that retain the essential localization and spreading properties of the phase-space distributions. These marginals allow for a direct comparison between the three representations and clarify how coarse graining, suppression of negativity, and smoothing influence the observable profiles of the quantum state.

For each (quasi)probability distribution $Q(x, p) \in \{W, |W|, H\}$, we define the position and momentum marginals by

$$Q_x(x) = \int_{-\infty}^{\infty} Q(x, p) dp, \quad Q_p(p) = \int_{-\infty}^{\infty} Q(x, p) dx. \quad (15)$$

For W , these marginals reproduce the exact quantum probability densities $|\psi(x)|^2$ and $|\phi(p)|^2$, while for $|W|$ and H they provide coarse-grained and smoothed analogues of these quantities.

5.1 Position Marginals

Figures 4–7 illustrate $Q_x(x)$ for the ground and first excited states. In Figs. 4 and 6 we adopt different scales on the axes to better highlight the overall form of the marginals, while in Figs. 5 and 7 we use a common scale to bring out additional structural details. Several general trends emerge across λ :

- **Wigner marginal** $W_x(x) = |\psi(x)|^2$. This is the only distribution that retains the nodal and parity structure of the true quantum state. For the ground state, $W_x(x)$ transitions from a single-peaked profile to a bimodal distribution as λ increases and the double well becomes pronounced. For the first excited state, the central node at $x = 0$ is preserved for all values of the coupling.
- **Modulus marginal** $|W|_x(x)$. Removing the sign structure from W causes the interference-induced dips in W_x to fill in. For $n = 0$, the two peaks appear earlier as λ increases, because $|W|$ enhances separated structures by eliminating destructive interference. For $n = 1$, the central depression is significantly reduced but not eliminated, since the antisymmetric shape of the state still influences the underlying geometry of W .
- **Husimi marginal** $H_x(x)$. This represents the most smoothed version of the position density. The transition from a single peak to a two-peak structure occurs at larger λ than in W_x or $|W|_x$, reflecting the smoothing imposed by Gaussian convolution. Even at large λ , the peaks of H_x remain significantly broader than those of W_x , showing that coarse graining suppresses sharp features related to tunneling-induced localization.

These differences highlight the role of negativity (present in W) and smoothing (present in H) in shaping the observable distribution along the x coordinate. The

modulus distribution $|W|_x$ provides an intermediate behaviour: it eliminates interference without erasing the structural splitting associated with the classical minima of the double-well potential.

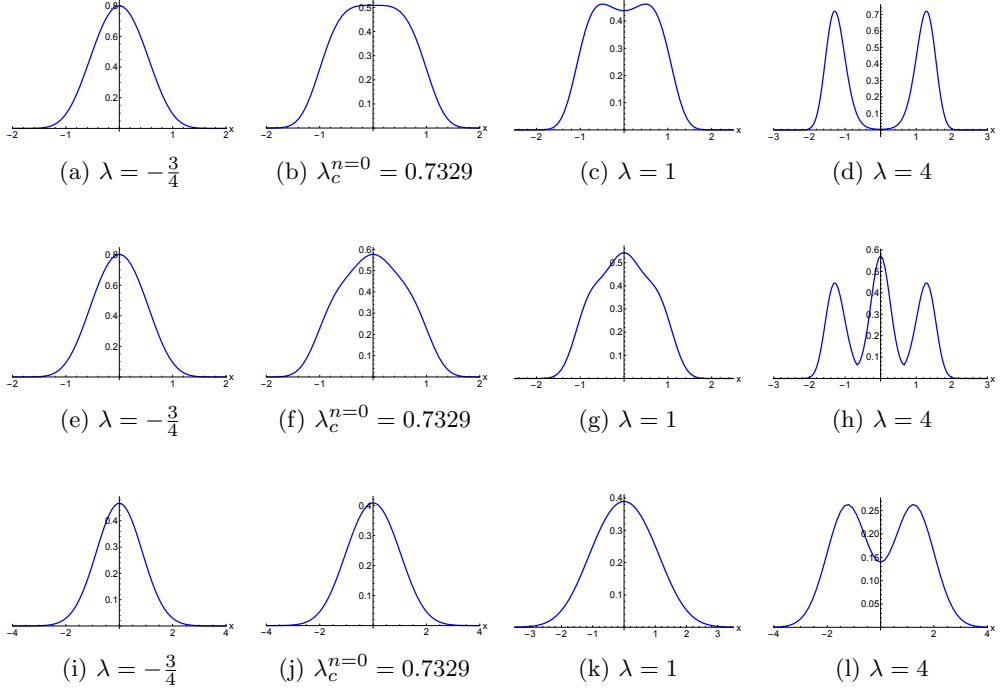


Fig. 4: Ground state $n = 0$. Position-space marginals Q_x of the three distributions: (a)–(d) Wigner function W , (e)–(h) its modulus $|W|$, and (i)–(l) the Husimi distribution H , shown for different values of the parameter λ .

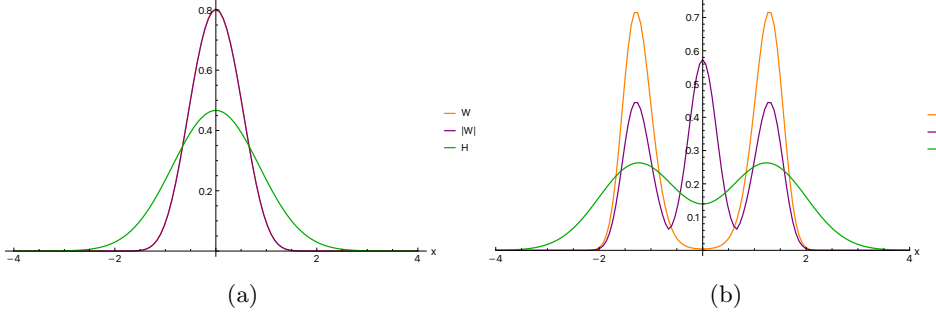


Fig. 5: Position-space marginals Q_x of W , $|W|$, and H for the ground state ($n = 0$), shown on a common scale for (a) $\lambda = -\frac{3}{4}$ and (b) $\lambda = 4$.

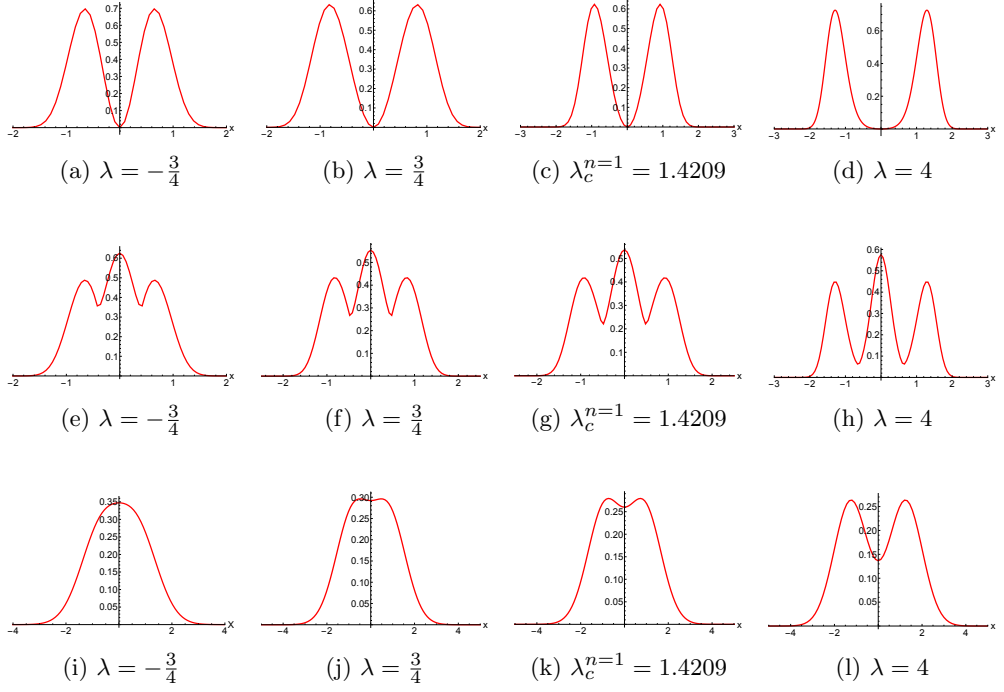


Fig. 6: First excited state $n = 1$. Position-space marginals Q_x of: (a)–(d) the Wigner function W , (e)–(h) its modulus $|W|$, and (i)–(l) the Husimi distribution H , for various values of λ .

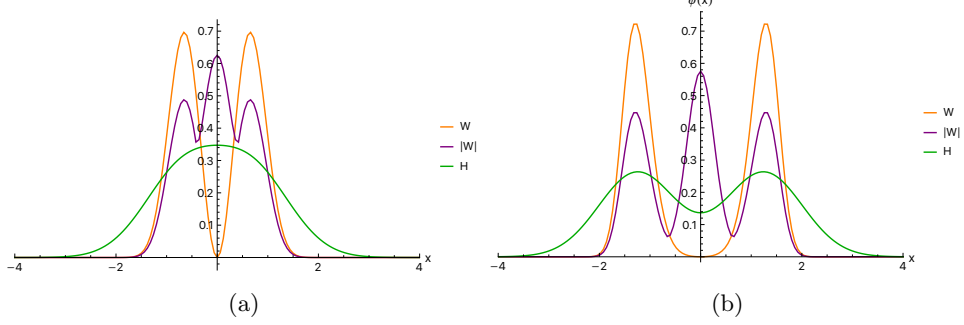


Fig. 7: Position-space marginals Q_x of W , $|W|$, and H for the first excited state ($n = 1$), shown on a common scale for (a) $\lambda = -\frac{3}{4}$ and (b) $\lambda = 4$.

5.2 Momentum Marginals

The momentum marginals $Q_p(p)$, shown in Figures 8-11, exhibit trends complementary to those observed in position space. In Figs. 8 and 10 we adopt different scales on the axes to better highlight the overall form of the marginals, while in Figs. 9 and 11 we use a common scale to bring out additional structural details. Some remarks are in order:

- **Wigner marginal** $W_p(p) = |\phi(p)|^2$. The momentum-space distributions reflect the Fourier-transform structure of $\psi(x)$, and therefore provide a sensitive probe of interference between separated spatial lobes. As λ increases and the state becomes more localized in position, $W_p(p)$ broadens and develops oscillations associated with coherent superpositions of left- and right-localized components.
- **Modulus marginal** $|W|_p(p)$. The removal of oscillatory signs reduces the amplitude of interference fringes in momentum space, but does not eliminate them entirely. For $n = 1$, the central dip at $p = 0$ is partially filled, reflecting the fact that the antisymmetric character of the state is less strongly encoded in $|W|$ than in W .
- **Husimi marginal** $H_p(p)$. This marginal is substantially smoother than the other two and typically exhibits a single broad peak for the ground state and a shallow central depression for the first excited state. The fine oscillatory structure present in $W_p(p)$ is entirely washed out, consistent with the coarse-grained nature of H .

As in position space, $H_p(p)$ gives the most classical-looking profile, while $W_p(p)$ retains the full oscillatory structure. The modulus distribution occupies an intermediate regime in which peak structure and overall width resemble those of W , but interference-induced oscillations are weakened.

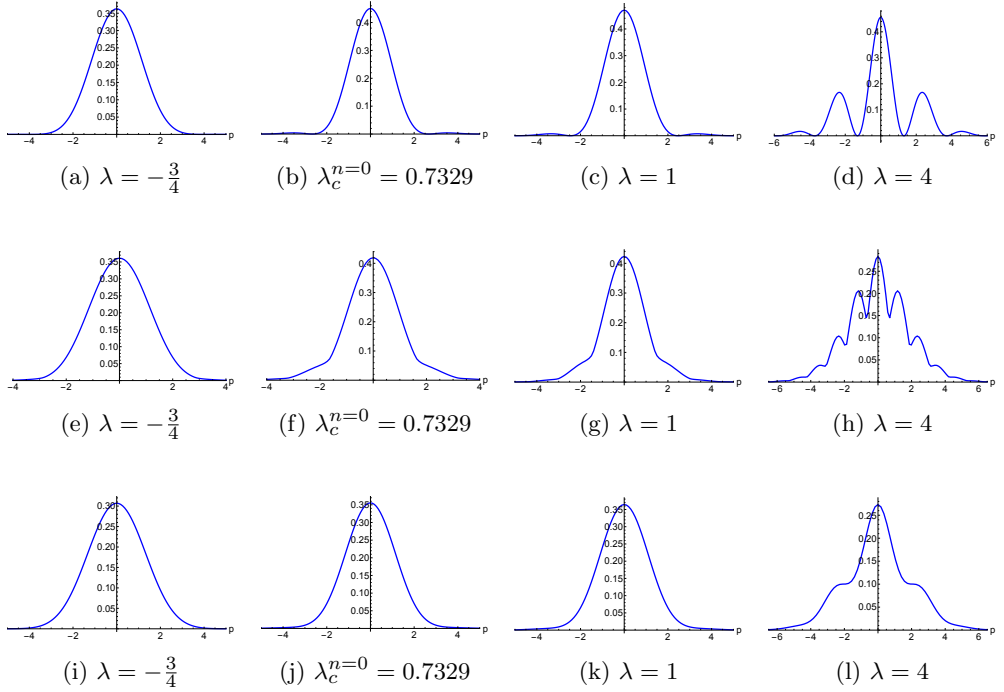


Fig. 8: Ground state $n = 0$. Momentum-space marginals Q_p of: (a)–(d) the Wigner function W , (e)–(h) its modulus $|W|$, and (i)–(l) the Husimi distribution H , shown for different values of λ .

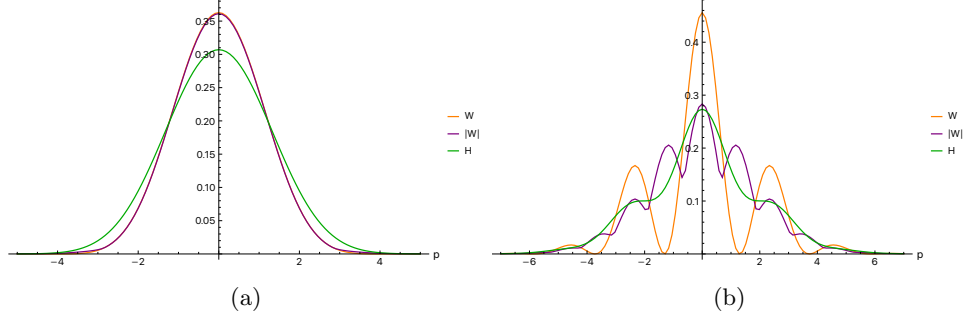


Fig. 9: Momentum-space marginals Q_p of W , $|W|$, and H for the ground state ($n = 0$), shown on a common scale for (a) $\lambda = -\frac{3}{4}$ and (b) $\lambda = 4$.

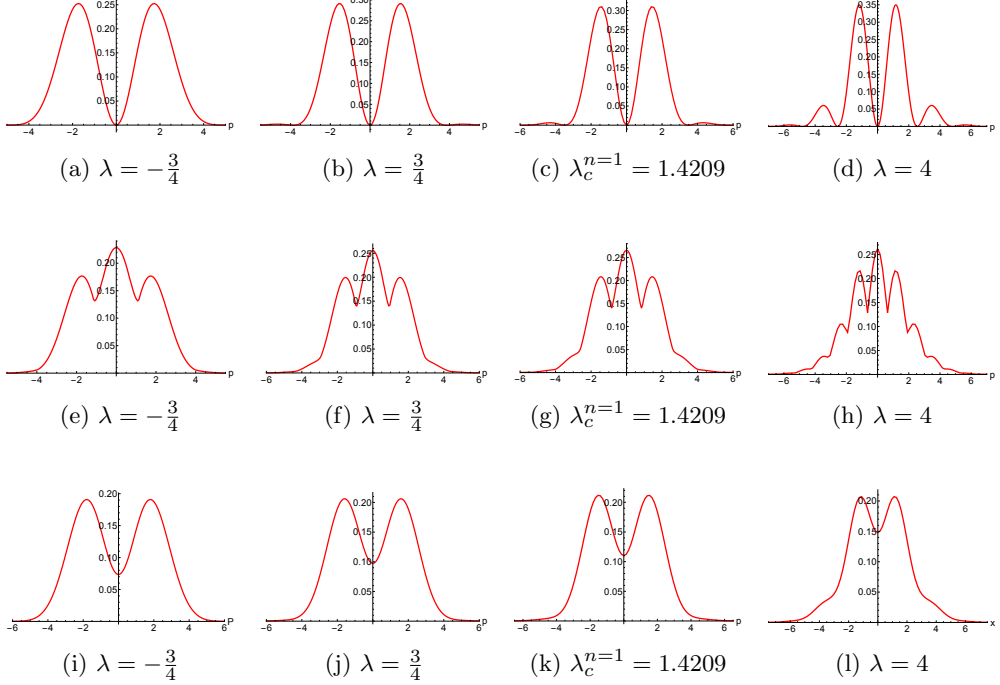


Fig. 10: First excited state $n = 1$. Momentum-space marginals Q_x of: (a)–(d) the Wigner function W , (e)–(h) its modulus $|W|$, and (i)–(l) the Husimi distribution H , shown for different values of λ .

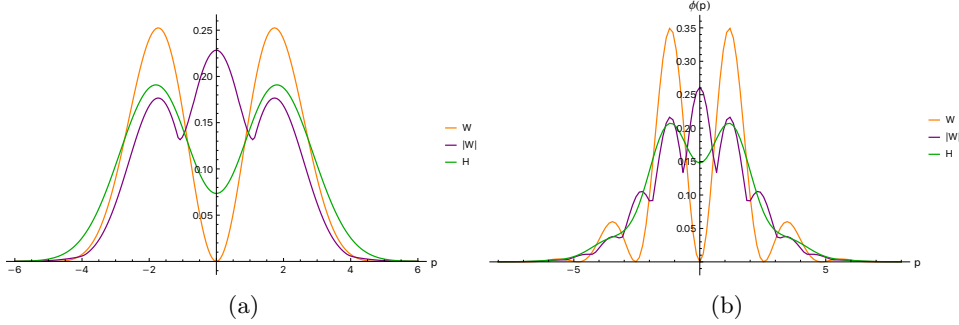


Fig. 11: Momentum-space marginals Q_p of W , $|W|$, and H for the first excited state ($n = 1$), shown on a common scale for (a) $\lambda = -\frac{3}{4}$ and (b) $\lambda = 4$.

5.3 Comparative interpretation

The systematic comparison of the marginals yields several general observations relevant to the later information-theoretic analysis:

- **Position marginals before tunneling ($\lambda \ll \lambda_c$):** For $n = 0$, all three marginals W_x , $|W|_x$, and H_x are nearly identical in structure (Fig. 4), each showing a single central peak. For $n = 1$, the three already differ (Fig. 6): W_x preserves the nodal structure at $x = 0$, $|W|_x$ partially fills the central dip but keeps a two-peak shape, and H_x produces the broadest, most smoothed profile. *For $n = 1$, the qualitative structure of W_x (one node, two lobes) remains unchanged with λ ; only the width, peak separation, and interference amplitude evolve, reflecting non-structural—rather than topological—modifications.*
- **Position marginals after tunneling ($\lambda > \lambda_c$):** Both states develop clear bimodality, and the three representations diverge (Figs. 4–6): W_x shows the sharpest peaks and most pronounced splitting, $|W|_x$ enhances the two-peak structure by removing destructive interference, and H_x delays and smooths the appearance of bimodality, giving the broadest double-humped distribution.
- **Momentum marginals before tunneling:** For $n = 0$, W_p , $|W|_p$, and H_p differ only slightly (Fig. 8): W_p and $|W|_p$ have similar widths, while H_p is slightly broader. For $n = 1$, W_p exhibits a central dip reflecting the spatial node (Fig. 10), $|W|_p$ partially fills this dip, and H_p yields a single smooth peak with minimal structure. *As in position space, the shape of W_p for $n = 1$ does not change qualitatively with λ ; the node in W_x simply translates into amplitude and width changes in W_p , not a modification of its underlying structure.*
- **Momentum marginals after tunneling:** For both states, W_p shows the strongest oscillatory structure due to left–right interference, $|W|_p$ retains a reduced remnant of these oscillations as strictly positive modulations, and H_p smooths them out almost completely (Figs. 8–10). The width of all marginals increases with λ , but the smoothing hierarchy is preserved.
- **Cross-state comparison:** After tunneling, $|W|_x$ and $|W|_p$ for $n = 0$ and $n = 1$ become more similar than the corresponding W or H marginals. Removing the sign structure erases the parity-induced contrast that remains visible in W_x , W_p , and, to a weaker extent, in the Husimi marginals.

These qualitative differences have direct consequences for the entropic and mutual-information measures studied in the next sections, where the marginals act as the primary inputs for quantifying the spreading, coherence, and structural complexity of the quantum state.

6 Entropic measures

Entropy-based quantities provide compact global indicators of the structural changes that the quasiprobability distributions undergo as the coupling parameter λ modifies the shape of the sextic potential. Since W , $|W|$, and H encode different degrees of smoothing and interference suppression, their entropies quantify, in a comparative and systematic way, how each representation captures delocalization, peak separation,

and the emergence of double-well structure. In this section we examine three types of entropy: the phase-space Shannon entropy computed directly from each quasiprobability, the position- and momentum-space entropies extracted from their marginals, and the combined total entropy $S_t = S_x + S_p$. In fact, S_t may be interpreted as the entropy of a separable phase-space distribution $Q(x, p) = Q_x(x)Q_p(p)$. When $Q(x, p) = W(x, p)$, this quantity is known as the Leipnik entropy [45].

The phase-space entropies are defined as

$$S[Q] = - \int_{-\infty}^{\infty} \int_{-\infty}^{\infty} Q(x, p) \ln Q(x, p) dx dp, \quad (16)$$

while the entropies of their marginals in position and in momentum space are

$$S_x[Q] = - \int_{-\infty}^{\infty} Q_x(x) \ln Q_x(x) dx, \quad S_p[Q] = - \int_{-\infty}^{\infty} Q_p(p) \ln Q_p(p) dp. \quad (17)$$

6.1 Shannon entropy

We begin by recalling that the quantity $S[W]$ does not constitute a strict Shannon entropy, since the Wigner function is not a bona fide probability density and may assume negative values. Rather, following the information-theoretic viewpoint adopted in the earlier work [8], $S[W]$ is best interpreted as a global delocalization functional defined directly on phase space. Within this framework, the real part $\text{Re } S_W$ provides a meaningful measure of the spatial and momentum spreading encoded in $W(x, p)$, while the imaginary component $\text{Im } S_W$ —which remains small across all values of λ considered here—acts as a sensitive indicator of sign-changing regions associated with interference and Wigner negativity. Moreover, the imaginary component is proportional to the volume of the negative regions in phase-space[13]. Note that this component increases with λ , illustrating that the volume of the negative regions also grows as λ increases.

Thus, even though $S[W]$ lacks the formal probabilistic status of $S[H]$ or of the one-dimensional Shannon entropies, its decomposition into real and imaginary parts yields complementary insights into phase-space structure, combining delocalization information with a diagnostic of quantum interference.

Figures 12 and 13 summarize the dependence of the phase-space Shannon entropy on λ for the ground and first excited states. Because the Wigner function can take negative values, its Shannon entropy may become complex valued; accordingly, Fig. 12 displays its real and imaginary parts. The real part grows with λ , reflecting the increased phase-space complexity associated with lobe separation and interference. The imaginary part remains small but nonzero, indicating the persistence of oscillatory regions where $W(x, p)$ changes sign. It is striking that there are broad minima in $\text{Re}(S[W])$, $|S[W]|$ and $S[H]$ in the ground state, but absent in $S[|W|]$. These roughly coincide in the regions around the λ critical point.

Figure 13 compares the entropy of the modulus $|W|$ with that of the Husimi distribution. Removing negativity consistently yields larger entropy in $|W|$, reflecting the enhancement of geometric peak separation once destructive interference has been

eliminated. The Husimi entropy is the largest across all regimes: Gaussian smearing broadens the distribution in both variables, maximizing uncertainty. These trends support a clear hierarchy across all values of λ ,

$$\text{Re}(S[W]) < |S[W]| < S[|W|] < S[H],$$

showing that each representation introduces a progressively stronger degree of smoothing. Also, there is an overall increasing tendency of the entropies with λ which can be interpreted as phase-space delocalization.

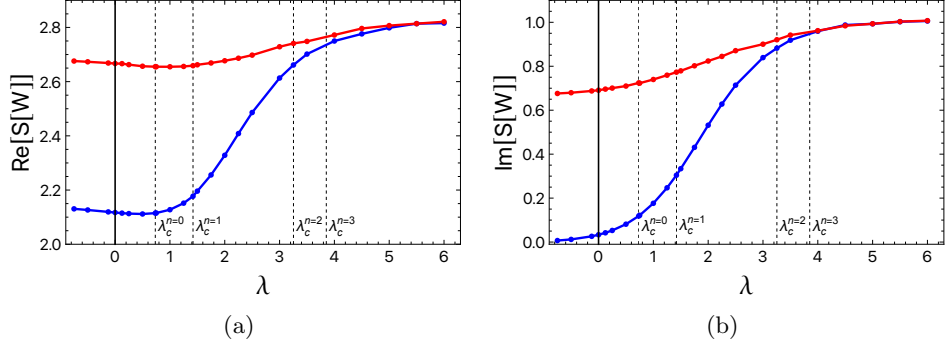


Fig. 12: Shannon entropy of the Wigner distribution for the ground $n = 0$ (blue curve) and first excited $n = 1$ (red curve) states as a function of λ . Panels (a)–(b) show $\text{Re } S_W$ and $\text{Im } S_W$, illustrating increased phase-space delocalization with λ .

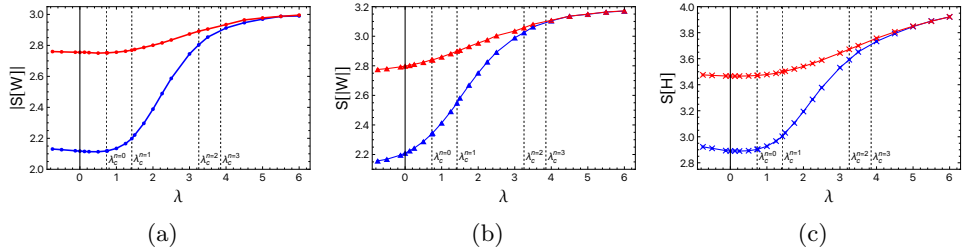


Fig. 13: Shannon entropy of the quasiprobability distributions vs. λ for the ground $n = 0$ (blue curve) and first excited $n = 1$ (red curve) states. Panels (a)–(c) display $|S[W]|$, $S[|W|]$ and $S[H]$, respectively, all showing increasing phase-space delocalization with λ .

6.2 Shannon entropies of marginals distributions

The position- and momentum-space entropies listed in Tables 1 and 2 provide a more detailed view of how localization evolves in each representation. For the Wigner function, $S_x[W]$ initially decreases as the potential narrows but increases again as the state becomes bimodal. The corresponding momentum entropy $S_p[W]$ follows the expected Fourier-dual trend: it increases whenever spatial localization becomes stronger.

For $|W|$, both S_x and S_p tend to be larger than the Wigner values. Eliminating interference fills in destructive dips and enhances the prominence of structural splitting, especially in the double-well regime. The Husimi entropies $S_x[H]$ and $S_p[H]$ are systematically the largest, reflecting the broadest and most smoothed marginals.

S_x				
Distributions	$\lambda = -\frac{3}{4}$	$\lambda_c^{n=0} = 0.7329$	$\lambda = 1$	$\lambda = 4$
W	0.669446	0.938019	0.993322	0.852065
$ W $	0.668119	0.917103	0.966693	1.15412
H	1.25773	1.36759	1.4004	1.70738
S_p				
Distributions	$\lambda = -\frac{3}{4}$	$\lambda_c^{n=0} = 0.7329$	$\lambda = 1$	$\lambda = 4$
W	1.48341	1.28365	1.2624	1.69748
$ W $	1.50555	1.4778	1.50888	2.00614
H	1.66566	1.54541	1.54159	2.05315

Table 1: Shannon Entropy in position and momentum space for some λ , $n = 0$

S_x				
Distributions	$\lambda = -\frac{3}{4}$	$\lambda = \frac{3}{4}$	$\lambda_c^{n=1} = 1.4209$	$\lambda = 4$
W	0.799305	0.894196	0.919881	0.828591
$ W $	0.907124	1.03248	1.08487	1.1505
H	1.44131	1.52491	1.56973	1.70813
S_p				
Distributions	$\lambda = -\frac{3}{4}$	$\lambda = \frac{3}{4}$	$\lambda_c^{n=1} = 1.4209$	$\lambda = 4$
W	1.81374	1.67882	1.63925	1.71753
$ W $	1.93029	1.87034	1.87503	2.01796
H	2.06706	1.98019	1.96378	2.07535

Table 2: Shannon Entropy in position and momentum space for some λ , $n = 1$

The Shannon entropies in Tables 1 and 2 quantify the smoothing hierarchy observed across the three representations. For all λ and for both $n = 0$ and $n = 1$, the ordering $S_x[W] < S_x[|W|] < S_x[H]$ (and likewise for S_p) holds consistently: for example, at $\lambda = 4$ in the ground state we find $S_x[W] = 0.852$, $S_x[|W|] = 1.154$, and $S_x[H] = 1.707$, with momentum entropies $S_p[W] = 1.697$, $S_p[|W|] = 2.006$, and $S_p[H] = 2.053$. Near the critical couplings $\lambda_c^{(0)} \approx 0.73$ and $\lambda_c^{(1)} \approx 1.42$, the position entropies reach clear minima, reflecting maximal spatial localization before the emergence of double-well splitting. The systematic increase of S_p with λ signals the stronger momentum-space oscillations associated with tunneling, while the consistently larger Husimi entropies highlight the extent to which Gaussian coarse-graining

broadens both position and momentum marginals. Collectively, these trends provide a quantitative backbone for the structural differences observed among W_n , $|W_n|$, and H_n .

Interestingly, the Fig. 14 shows that the maximum in $S_x[W]$ is also present in $S_x[|W|]$, but not in $S_x[H]$. This illustrates how the structure present in the Wigner-based distributions is largely washed out in the Husimi distribution. On the other hand, the minimum in $S_p[Q]$ appears in all three cases.

6.3 Total Shannon entropy

The total entropy

$$S_t = S_x + S_p, \quad (18)$$

provides a single measure of global spreading in the x - p plane. The behavior shown in Fig. 14 reflects the same hierarchical smoothing already observed in the individual marginals. For both quantum states, S_t increases with λ , indicating that the transition to a double-well configuration introduces additional complexity in both conjugate variables. Once again, the Wigner function marginals yield the smallest entropy sum, $|W|$ gives intermediate values, and the Husimi function produces the broadest distributions and largest uncertainties. Finally, $S_t[H]$ exhibits a minimum that is not present in the other two (quasi)distributions.

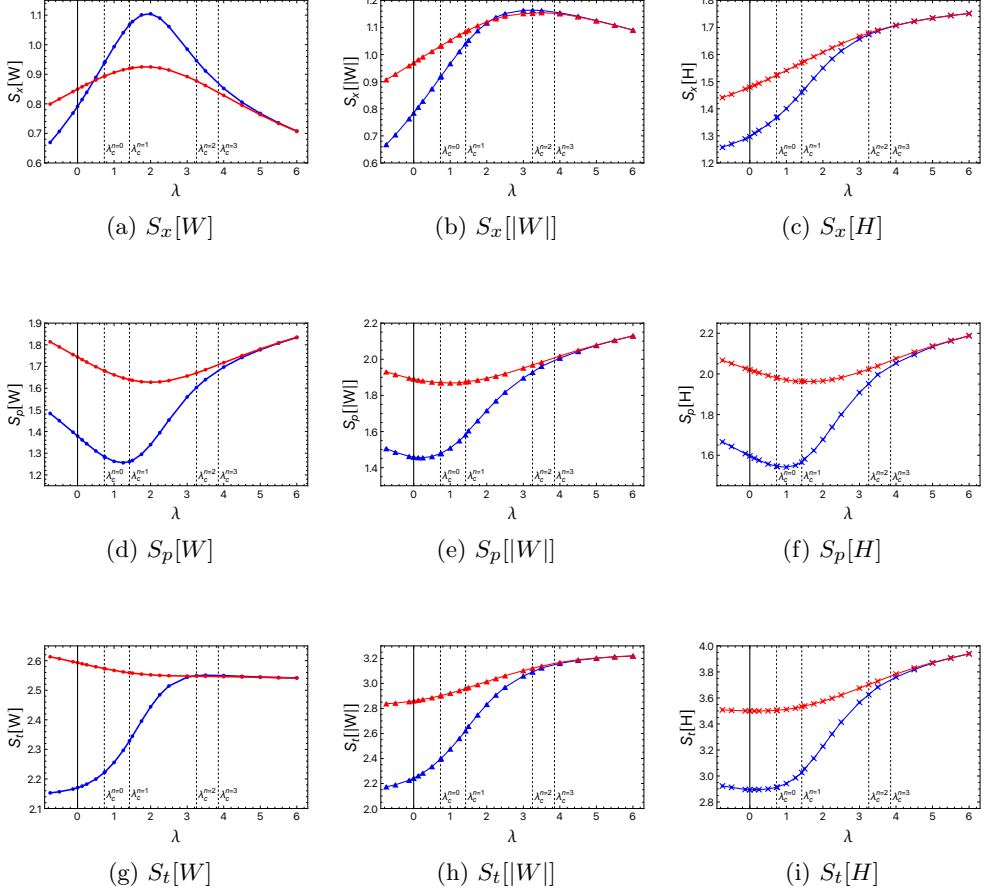


Fig. 14: Position, momentum, and total entropies S_x , S_p , and S_t versus λ for $n = 0$ (blue curve) and $n = 1$ (red curve), showing the consistent hierarchy $S[W_n] < S[|W_n|] < S[H_n]$ and the growth of global spreading as the potential evolves toward a double-well shape.

Mutual information quantifies the statistical dependence between position and momentum in a given phase-space representation. Since W , $|W|$, and H encode different amounts of interference, smoothing, and geometric structure, the corresponding values of I_Q reflect how strongly each quasiprobability couples the variables x and p . It is defined as

$$I_Q = \int_{-\infty}^{\infty} \int_{-\infty}^{\infty} Q(x, p) \ln \left[\frac{Q(x, p)}{Q_x(x) Q_p(p)} \right] dx dp = S_x[Q] + S_p[Q] - S[Q], \quad (19)$$

so that larger values indicate a greater departure from a factorized, product form of the phase-space distribution.

Figure 15 shows $I_Q(\lambda)$ for the three representations and the two lowest states. Only the real part of I_W is displayed, as its imaginary component is the negative of $\text{Im}[S[W]]$ presented in Fig. 12. For the Wigner function, I_W increases monotonically as the system evolves from a single well to a double well, reflecting the strengthening of x - p correlations induced by spatial separation and the associated interference fringes, which sharpen near and beyond the critical couplings $\lambda_c^{(n)}$.

For $|W|$, the removal of negativity suppresses the finest oscillations while preserving the underlying bimodal geometry. The resulting $I_{|W|}$ therefore lies between the Wigner and Husimi values: reduced relative to W yet still substantially larger than I_H . This indicates that geometric localization alone produces appreciable x - p dependence even in the absence of interference.

The Husimi function, shaped by Gaussian coarse graining, yields the smallest mutual information. Here the joint entropy S grows faster than the marginals S_x and S_p , leaving only broad semiclassical correlations. The hierarchy

$$\text{Re}[I_W] > I_{|W|} > I_H$$

thus captures how interference, geometric splitting, and smoothing generate strong, intermediate, and weak phase-space correlations. All three $I_Q(\lambda)$ curves exhibit maxima in the ground state, though not at the same coupling values.

This ordering also has a structural interpretation. Mutual information measures the departure from a separable portrait $Q(x, p) = Q_x(x)Q_p(p)$ and therefore characterizes an entanglement-like nonseparability between x and p . Interference fringes and multimodal structures in $W(x, p)$ introduce multiple relevant spatial scales, producing the largest effective correlation dimension. The modulus $|W|$ retains only the geometric splitting and therefore yields an intermediate dimension, while the Husimi function is dominated by a single smooth, semiclassical scale. This behavior parallels the entropy hierarchy

$$S[W] < S[|W|] < S[H],$$

and confirms that the transition to the double-well regime enhances both the nonseparability of the phase-space variables and the structural complexity of the quasiprobability representations.

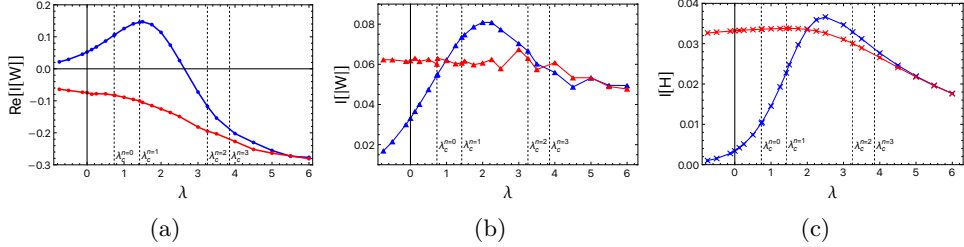


Fig. 15: Mutual information I of the (quasi)probability distributions: (a) W , (b) $|W|$ and (c) H as a function of the coupling parameter λ for the ground $n = 0$ (blue curve) and first excited $n = 1$ (red curve) states.

6.4 Cumulative Residual Jeffreys (CRJ) Divergence

The Cumulative Residual Jeffreys (CRJ) divergence provides a symmetric and numerically stable measure of dissimilarity between two probability densities ρ_m and ρ_n [46]. For any density ρ_n , we define the associated survival (cumulative–residual) function $S_n(x) = \int_x^\infty \rho_n(t) dt$, and analogously for $S_m(x)$. The CRJ divergence is then given by

$$D_{\text{CRJ}}(\rho_m \parallel \rho_n) = \int_{-\infty}^{\infty} S_n(x) \ln\left(\frac{S_n(x)}{S_m(x)}\right) dx + \int_{-\infty}^{\infty} S_m(x) \ln\left(\frac{S_m(x)}{S_n(x)}\right) dx, \quad (20)$$

which is manifestly symmetric under $\rho_m \leftrightarrow \rho_n$. Unlike the KL divergence, D_{CRJ} remains finite even when the densities possess different supports or nodal structures, since it compares their *tails* rather than their pointwise values.

In the present context, we use D_{CRJ} to quantify how strongly the marginals of the modulus distribution $|W|$ and the Husimi distribution H deviate from those of the Wigner function W , in both position and momentum space. Because these three quasiprobabilities differ in their treatment of negativity, interference, and Gaussian smoothing, the CRJ divergence provides a precise and robust diagnostic of how these structural differences manifest in their one-dimensional marginals.

Tables 3 and 4 summarize the divergences for the ground and first excited states across representative values of λ . Several clear trends emerge:

- **Near-coincidence of $|W_n|$ and W_n at low coupling.** For small λ , $D_{\text{CRJ}}(|W_n|, W_n)$ is extremely small (e.g., 9.7×10^{-7} in x for $n = 0$ at $\lambda = -\frac{3}{4}$), showing that sign removal barely affects the Wigner marginals.
- **Steady growth of $D_{\text{CRJ}}(|W_n|, W_n)$ with well formation.** As λ increases and the double well develops, the divergences rise (e.g., $\approx 1.3 \times 10^{-1}$ in x at $\lambda = 4$), reflecting enhanced interference and lobe separation.
- **CRJ as a tunneling indicator.** The monotonic increase of D_{CRJ} tracks the emergence of left–right coherence and the suppression of interference under smoothing.

- **Largest deviations for Husimi marginals.** Husimi smoothing produces the strongest departures from W . For $n = 0$, $D_{CRJ}(H_n, W_n)$ grows from 0.351 to 0.595 as λ increases from $-\frac{3}{4}$ to 4, roughly an order of magnitude larger than the corresponding $|W_n| - W_n$ values.
- **Consistently smaller divergences in momentum space.** Momentum-space divergences remain low (typically $\lesssim 0.07$), reflecting the weaker oscillatory structure of the momentum marginals and the reduced impact of Husimi smoothing in p .
- **Greater sensitivity of the first excited state.** The nodal structure of $n = 1$ yields systematically larger divergences, e.g., $D_{CRJ}(|W_1|, W_1) = 0.133$ and $D_{CRJ}(H_1, W_1) = 0.580$ at $\lambda = 4$, exceeding the corresponding ground-state values.

Position space						
$D_{CRJ}(\rho_m \rho_n)$	$\lambda = -\frac{3}{4}$	$\lambda_c^{n=0} = 0.7329$	$\lambda = 1$	$\lambda = 2.5$	$\lambda = 4$	$\lambda = 5$
(W , W)	9.72868×10^{-7}	0.000839818	0.00214324	0.0579798	0.131541	0.157213
(H, W)	0.350672	0.287128	0.28866	0.431972	0.595489	0.638869
(H, W)	0.346475	0.301167	0.308648	0.488934	0.672753	0.726098
Momentum space						
$D_{CRJ}(\rho_m \rho_n)$	$\lambda = -\frac{3}{4}$	$\lambda_c^{n=0} = 0.7329$	$\lambda = 1$	$\lambda = 2.5$	$\lambda = 4$	$\lambda = 5$
(W , W)	0.00289026	0.0434621	0.0589254	0.0757902	0.0431918	0.0337971
(H, W)	0.0476579	0.0658988	0.0667597	0.0491116	0.0369542	0.0325187
(H, W)	0.0333811	0.0880575	0.00589606	0.00879494	0.00853151	0.00753547

Table 3: CRJ divergences for the ground state ($n = 0$) in position and momentum space for selected values of λ .

Position space						
$D_{CRJ}(\rho_m \rho_n)$	$\lambda = -\frac{3}{4}$	$\lambda = \frac{3}{4}$	$\lambda_c^{n=1} = 1.4209$	$\lambda = 2.5$	$\lambda = 4$	$\lambda = 5$
(W , W)	0.0390777	0.0518047	0.063286	0.0910459	0.13334	0.157484
(H, W)	0.394839	0.40362	0.425713	0.492836	0.579705	0.637086
(H, W)	0.432782	0.462339	0.485834	0.558428	0.657533	0.724503
Momentum space						
$D_{CRJ}(\rho_m \rho_n)$	$\lambda = -\frac{3}{4}$	$\lambda = \frac{3}{4}$	$\lambda_c^{n=1} = 1.4209$	$\lambda = 2.5$	$\lambda = 4$	$\lambda = 5$
(W , W)	0.101457	0.0816687	0.0735118	0.059317	0.0417442	0.0333961
(H, W)	0.0459038	0.0542097	0.0541598	0.0471514	0.0372011	0.0319676
(H, W)	0.122977	0.078894	0.0488316	0.0225922	0.00993492	0.00765889

Table 4: CRJ divergences for the first excited state ($n = 1$) in position and momentum space for selected values of λ .

7 Key Findings

This study presented a systematic comparison of three phase-space representations of a quantum state—the Wigner function $W(x, p)$, its modulus $|W(x, p)|$, and the Husimi distribution $H(x, p)$ —using the quasi-exactly solvable (QES) sextic potential as a model system. Our analysis, based on variational wavefunctions for the ground and first excited states, led to the following three main discoveries:

1. **Intermediate Role of the Modulus-Wigner Function:** The modulus of the Wigner function, $|W(x, p)|$, provides a meaningful intermediate phase-space representation. It preserves the geometric structure and localization features of the

quantum state while eliminating the sign-changing interference fringes present in the original Wigner function. This representation bridges the detailed, oscillatory Wigner function and the smoothed, positive-definite Husimi distribution.

2. **Hierarchical Ordering of Coherence and Delocalization:** Shannon entropy and mutual information analyses reveal a consistent hierarchy across the three phase-space distributions. The Wigner function shows the strongest coherence and sharpest localization (lowest entropy, highest mutual information), followed by $|W(x, p)|$, with the Husimi function displaying the most delocalization and weakest correlations. This ordering— $W > |W| > H$ —holds across the transition from single- to double-well regimes.
3. **CRJ Divergence as a Diagnostic Tool:** The Cumulative Residual Jeffreys (CRJ) divergence was introduced as a robust and symmetric metric to quantify differences between phase-space representations. It effectively tracks tunneling-induced changes, with $D_{\text{CRJ}}(H, W)$ increasing significantly as the double-well structure emerges. In contrast, $|W|$ remains closer to W , confirming its utility as a structure-preserving yet interference-filtering alternative.

The distinct ability of the three Shannon entropies to capture the structural transition is summarized in Table 5.

Table 5: Sensitivity of Shannon entropies to the single- to double-well transition and the onset of tunneling.

Entropy	Well splitting	Tunneling / interference	Transition signature
$S[W]$	Strong	Strong	Nonmonotonic, sharp
$S[W]$	Moderate	None	Smooth, monotonic
$S[H]$	Weak	None	Broad, featureless

8 Conclusions

The comparative framework developed in this work sheds light on the structure, coherence, and delocalization properties encoded in different phase-space representations of quantum states. We showed that while the Wigner function offers a complete picture including quantum interference, the modulus-Wigner and Husimi distributions provide progressively smoothed alternatives, useful for emphasizing geometric structure or classical correspondence.

The hierarchy $W > |W| > H$ appears to be a general feature in systems where coherence and classicality compete, such as double-well and tunneling configurations. In particular, the $|W|$ function emerges as a valuable compromise, retaining fine structure without interference, and the CRJ divergence serves as a sensitive indicator of structural changes and information loss.

These insights have broader implications for phase-space methods in atomic, molecular, optical, and condensed-matter systems. Potential applications include quantum control, decoherence monitoring, and nonclassical state characterization. The tools demonstrated here—especially the use of entropy, mutual information, and CRJ divergence—are broadly applicable to analyzing localization, spreading, and the emergence of classicality in quantum systems.

Moreover, the present results provide a general framework for assessing the information-theoretic sensitivity of phase-space representations in systems with emerging tunneling and bimodality.

This framework can be extended to time-dependent dynamics to study how phase-space coherence and structure evolve under tunneling, interference, and decoherence. Applying the same tools to higher excited states or to other quasi-exactly solvable and anharmonic potentials could test the universality of the observed trends. Further comparisons with alternative quasiprobability distributions (e.g., Glauber–Sudarshan P or Kirkwood–Rihaczek) may also deepen our understanding of quantum–classical transitions in diverse physical settings.

Funding declaration

A. M. Escobar Ruiz would like to thank the support from Consejo Nacional de Humanidades, Ciencias y Tecnologías (CONAHCyT, now Secihto) of Mexico under Grant CF-2023-I-1496 and from UAM research grant DAI 2024-CPIR-0. A. N. Mendoza Tavera wishes to thank Secihto (México) for the financial support provided through a doctoral scholarship.

Data availability

Data sharing is not applicable to this article as no new data were created or analyzed in this study.

References

- [1] Wigner, E.P.: On the quantum correction for thermodynamic equilibrium. *Phys.*

Rev. **40**, 749 (1932) <https://doi.org/10.1103/PhysRev.40.749>

- [2] Husimi, K.: Some formal properties of the density matrix. Proc. Phys. Math. Soc. Jpn. **22**, 264 (1940) <https://doi.org/10.11429/ppmsj1919.22.4.264>
- [3] Imhof, E., Stickney, J., Squires, M.: A Wigner function approach to coherence in a Talbot–Lau interferometer. Atoms **4**(2), 18 (2016) <https://doi.org/10.3390/atoms4020018>
- [4] Casado, A., Guerra, S., Plácido, J.: From Stochastic Optics to the Wigner formalism. Atoms **7**(3), 76 (2019) <https://doi.org/10.3390/atoms7030076>
- [5] Dimitrijević, M.S., Srećković, V.A., Zalam, A.A., Bezuglov, N.N., Klyucharev, A.N.: Dynamic instability of Rydberg atomic complexes. Atoms **7**(1), 22 (2019) <https://doi.org/10.3390/atoms7010022>
- [6] Abgaryan, V., Khvedelidze, A.: On families of Wigner functions for N-level quantum systems. Symmetry **13**(6), 1013 (2021) <https://doi.org/10.3390/sym13061013>
- [7] Connerade, J.-P.: The Atom at the Heart of Physics. Atoms **11**(2), 32 (2023) <https://doi.org/10.3390/atoms11020032>
- [8] Laguna, H.G., Sagar, R.P.: Shannon entropy of the Wigner function. Int. J. Quantum Inf. **8**, 1089 (2010) <https://doi.org/10.1142/S0219749910006484>
- [9] Wehrl, A.: On the relation between classical and quantum-mechanical entropy. Rep. Math. Phys. **16**, 353 (1979) [https://doi.org/10.1016/0034-4877\(79\)90070-3](https://doi.org/10.1016/0034-4877(79)90070-3)
- [10] Calixto, M., Real, R., Romera, E.: Husimi distribution and phase-space analysis of a vibron-model quantum phase transition. Phys. Rev. A **86**, 032508 (2012) <https://doi.org/10.1103/PhysRevA.86.032508>
- [11] Floerchinger, S., Haas, T., Müller-Groeling, H.: Wehrl entropy, entropic uncertainty relations, and entanglement. Phys. Rev. A **103**, 062222 (2021) <https://doi.org/10.1103/PhysRevA.103.062222>
- [12] Kazandjian, L., Soubiran, F., Pain, J.-C.: On the Wigner–Kirkwood expansion of the free energy and the evaluation of the quantum correction. Atoms **10**(2), 65 (2022) <https://doi.org/10.3390/atoms10020065>
- [13] Salazar, S.J.C., Laguna, H.G., Sagar, R.P.: Phase-space quantum distributions and information theory. Phys. Rev. A **107**, 042417 (2023) <https://doi.org/10.1103/PhysRevA.107.042417>
- [14] Smith, A., Sinha, K., Jarzynski, C.: Quantum coherences and classical inhomogeneities as equivalent thermodynamics resources. Entropy **24**(4), 474 (2022) <https://doi.org/10.3390/e24040474>

- [15] Yamada, S., Kobayashi, T., Takahata, M., Nitta, H., Isobe, H., Kawakami, T., Yamanaka, S., Okumura, M., Yamaguchi, K.: Non-perturbative approaches to linear and nonlinear responses of atoms, molecules, and molecular aggregates: A theoretical approach to molecular quantum information and quantum biology. *Chemistry* **7**(5), 164 (2025) <https://doi.org/10.3390/chemistry7050164>
- [16] Gadre, S.R., Sears, S.B., Chakravorty, S.J., Bendale, R.D.: Some novel characteristics of atomic information entropies. *Phys. Rev. A* **32**, 2602 (1985) <https://doi.org/10.1103/PhysRevA.32.2602>
- [17] Bialynicki-Birula, I.: Formulation of the uncertainty relations in terms of the Rényi entropies. *Phys. Rev. A* **74**, 052101 (2006) <https://doi.org/10.1103/PhysRevA.74.052101>
- [18] Nagy, A., Romera, E.: Relation between Fisher measures of information coming from pair distributions. *Chem. Phys. Lett.* **490**, 242 (2010) <https://doi.org/10.1016/j.cplett.2010.03.057>
- [19] Angulo, J.C., Antolín, J.: Atomic complexity measures in position and momentum spaces. *J. Chem. Phys.* **128**, 164109 (2008) <https://doi.org/10.1063/1.2907743>
- [20] Anteneodo, C., Plastino, A.R.: Lmc complexity. *Phys. Lett. A* **223**, 348 (1996) [https://doi.org/10.1016/S0375-9601\(96\)00756-6](https://doi.org/10.1016/S0375-9601(96)00756-6)
- [21] Nagy, A.: Phase-space Rényi entropy, complexity and thermodynamic picture. *J. Math. Chem.* **61**, 296 (2023) <https://doi.org/10.1007/s10910-022-01347-6>
- [22] Tsallis, C.: Possible generalization of Boltzmann-Gibbs statistics. *J. Stat. Phys.* **52**, 479 (1988) <https://doi.org/10.1007/BF01016429>
- [23] Flores-Gallegos, N.: Tsallis entropy as a possible measure of the electron correlation in atomic systems. *Chem. Phys. Lett.* **692**, 61 (2018) <https://doi.org/10.1016/j.cplett.2017.12.014>
- [24] Kutzelnigg, W., Del Re, G., Berthier, G.: Correlation coefficients for electronic wave functions. *Phys. Rev.* **172**, 49 (1968) <https://doi.org/10.1103/PhysRev.172.49>
- [25] Thakkar, A.J., Smith, V.H.: Statistical electron correlation coefficients for helium-like ions. *Phys. Rev. A* **23**, 473 (1981) <https://doi.org/10.1103/PhysRevA.23.473>
- [26] Laguna, H.G., Sagar, R.P.: Position-momentum correlations in the Moshinsky atom. *J. Phys. A* **45**, 025307 (2011) <https://doi.org/10.1088/1751-8113/45/2/025307>
- [27] Laguna, H.G., Sagar, R.P.: Statistical correlations in the Moshinsky atom. *Phys.*

Rev. A **84**, 012502 (2011) <https://doi.org/10.1103/PhysRevA.84.012502>

- [28] Matsuda, H.: Physical nature of higher-order mutual information. Phys. Rev. E **62**, 3096 (2000) <https://doi.org/10.1103/PhysRevE.62.3096>
- [29] Salazar, S.J.C., Laguna, H.G., Sagar, R.P.: Higher-order statistical correlations in three-particle quantum systems with harmonic interactions. Phys. Rev. A **101**, 042505 (2020) <https://doi.org/10.1103/PhysRevA.101.042105>
- [30] Salazar, S.J.C., Laguna, H.G., Sagar, R.P.: Mutual-information sums and relations with interaction energies. Phys. Rev. E **110**, 034133 (2024) <https://doi.org/10.1103/PhysRevE.110.034133>
- [31] Moustakidis, C.C., Chatzisavvas, K.C., Panos, C.P.: Quantum-information properties of nuclei and trapped Bose gases. Int. J. Mod. Phys. E **14**, 1087 (2005) <https://doi.org/10.1142/S0218301305003739>
- [32] Sriraman, T., Chakrabarti, B., Trombettoni, A., Muruganandam, P.: Characteristic features of the Shannon information entropy of dipolar BEC. J. Chem. Phys. **147**, 044304 (2017) <https://doi.org/10.1063/1.4994922>
- [33] Zhao, Q., Zhao, J.: Optical lattice effects on Shannon information entropy in rotating BEC. J. Low Temp. Phys. **194**, 302 (2019) <https://doi.org/10.1007/s10909-018-2099-5>
- [34] Chakrabarti, B., Gammal, A., Chavda, N.D., Lekala, M.L.: Quantum-information-theoretic measures to distinguish fermionized bosons. Phys. Rev. A **109**, 063308 (2024) <https://doi.org/10.1103/PhysRevA.109.063308>
- [35] Flores-Gallegos, N., Flores-Gómez, L.: An approach to chemical hardness through Shannon's entropy. J. Math. Chem. **61**, 1726 (2023) <https://doi.org/10.1007/s10910-023-01488-2>
- [36] Romera, E., Santos, F.: Identifying Wave-Packet Fractional Revivals by Means of Information Entropy. Phys. Rev. Lett. **99**, 263601 (2007) <https://doi.org/10.1103/PhysRevLett.99.263601>
- [37] Turbiner, A.V.: Quasi-exactly solvable problems and $sl(2)$ algebra. Commun. Math. Phys. **118**, 467 (1988) <https://doi.org/10.1007/BF01466727>
- [38] Turbiner, A.V., Ushveridze, A.G.: Spectral singularities and quasi-exactly solvable quantal problem. Phys. Lett. A **126**, 181 (1987) [https://doi.org/10.1016/0375-9601\(87\)90456-7](https://doi.org/10.1016/0375-9601(87)90456-7)
- [39] Ushveridze, A.G.: Exact solutions of Schrödinger equations. Sov. Phys.–Lebedev Inst. Rep. **2**, 54 (1988)
- [40] Bender, C.M., Dunne, G.V.: Quasi-exactly solvable systems and orthogonal

polynomials. *J. Math. Phys.* **37**, 6 (1996) <https://doi.org/10.1063/1.531373>

[41] Contreras-Astorga, A., Escobar-Ruiz, A.M.: QES sextic and Morse potentials: SUSY and WKB. *J. Phys. Conf. Ser.* **2986**, 012010 (2025) <https://doi.org/10.1088/1742-6596/2986/1/012010>

[42] Contreras-Astorga, A., Escobar-Ruiz, A.M., Linares, R.: Supersymmetric partners of the QES sextic revisited. *Phys. Scr.* **99**, 025223 (2024) <https://doi.org/10.1088/1402-4896/ad1913>

[43] Mendoza Tavera, A.N., Escobar Ruiz, A.M., Sagar, R.P.: Entropic characterization of tunneling and state pairing in a QES sextic potential. *Int. J. Theor. Phys.* (2025) <https://doi.org/10.1007/s10773-025-06189-x>

[44] Valle, J.C.: Solving the one-dimensional time-independent Schrödinger equation with high accuracy: The LagrangeMesh Mathematica® package. *International Journal of Modern Physics C* **35**(01), 2450011 (2024) <https://doi.org/10.1142/S0129183124500116>

[45] Leipnik, R.: The extended entropy uncertainty principle. *Information and Control* **3**(1), 18–25 (1960) [https://doi.org/10.1016/S0019-9958\(60\)90227-8](https://doi.org/10.1016/S0019-9958(60)90227-8)

[46] Laguna, H.G., Salazar, S.J.C., Sagar, R.P.: Entropic Kullback-Leibler type distance measures for quantum distributions. *International Journal of Quantum Chemistry* **119**(19), 25984 (2019) <https://doi.org/10.1002/qua.25984> <https://onlinelibrary.wiley.com/doi/pdf/10.1002/qua.25984>

A Algebraic QES structure of the sextic potential

In this Appendix, we summarize the Lie-algebraic foundation underlying the quasi-exact solvability of the sextic potential [37]. For a discrete set of couplings $\lambda = N \in \mathbb{N}$, the Schrödinger operator can be gauge-rotated into an element of the universal enveloping algebra of $\mathfrak{sl}(2, \mathbb{R})$ acting on a finite-dimensional polynomial space, yielding $(N + 1)$ exact even-parity eigenstates.

A.1 Rescaled Hamiltonian and gauge factor

The Hamiltonian is

$$H = -\frac{1}{2} \frac{d^2}{dx^2} + \frac{1}{2} (x^6 + 2x^4 - 2(2\lambda + 1)x^2), \quad (21)$$

and we rescale

$$\tilde{H} = 2H = -\frac{d^2}{dx^2} + x^6 + 2x^4 - 2(2\lambda + 1)x^2. \quad (22)$$

We perform the gauge transformation

$$\psi(x) = e^{-g(x)} P(x), \quad g(x) = \frac{x^4}{4} + \frac{x^2}{2}, \quad (23)$$

and define the gauge-rotated operator

$$h = e^g \tilde{H} e^{-g}. \quad (24)$$

A direct calculation gives

$$h = -\frac{d^2}{dx^2} + 2(x^3 + x) \frac{d}{dx} + (1 - 4\lambda x^2). \quad (25)$$

The original eigenvalue problem becomes

$$h P(x) = E P(x), \quad (26)$$

with $P(x)$ a function to be determined.

A.2 Even sector and change of variable $z = x^2$

For even-parity states we write

$$z = x^2, \quad P(x) = \Phi(z), \quad (27)$$

so that

$$\frac{d}{dx} = 2x \frac{d}{dz}, \quad \frac{d^2}{dx^2} = 2 \frac{d}{dz} + 4z \frac{d^2}{dz^2}. \quad (28)$$

Substituting these into (25) yields an operator acting on $\Phi(z)$:

$$h = -4z \frac{d^2}{dz^2} + (4z^2 + 4z - 2) \frac{d}{dz} + (1 - 4\lambda z). \quad (29)$$

A.3 $\mathfrak{sl}(2)$ generators and the QES condition

Let

$$\mathcal{P}_N = \{1, z, z^2, \dots, z^N\}, \quad (30)$$

and consider the differential realization of $\mathfrak{sl}(2, \mathbb{R})$ on \mathcal{P}_N :

$$J_- = \frac{d}{dz}, \quad J_0 = z \frac{d}{dz} - \frac{N}{2}, \quad J_+ = z^2 \frac{d}{dz} - Nz, \quad (31)$$

which satisfy

$$[J_0, J_{\pm}] = \pm J_{\pm}, \quad [J_+, J_-] = -2J_0. \quad (32)$$

These generators map \mathcal{P}_N into itself, so any polynomial expression in $\{J_+, J_0, J_-\}$ preserves \mathcal{P}_N .

To see the quasi-exact solvability, we examine the action of (29) on a highest-degree monomial z^N . The potentially degree-raising term in $h z^N$ is proportional to z^{N+1} with coefficient

$$4N - 4\lambda, \quad (33)$$

which vanishes precisely when

$$\lambda = N \in \mathbb{N}. \quad (34)$$

Thus, for these discrete couplings, h preserves \mathcal{P}_N .

Moreover, one can express h as a quadratic element of the universal enveloping algebra $U(\mathfrak{sl}(2, \mathbb{R}))$. For $\lambda = N$ one finds explicitly

$$h = 4J_+ - 4J_0 J_- + (-2N - 2) J_- + 4J_0 + (2N + 1) \mathbb{I}, \quad (35)$$

which acts invariantly on \mathcal{P}_N , i.e.

$$h : \mathcal{P}_N \longrightarrow \mathcal{P}_N. \quad (36)$$

The eigenvalue problem

$$h\Phi(z) = E\Phi(z), \quad \Phi(z) \in \mathcal{P}_N, \quad (37)$$

reduces to diagonalizing a finite $(N + 1) \times (N + 1)$ matrix. Therefore, for $\lambda = N$ the sextic oscillator possesses exactly $(N + 1)$ even algebraic eigenstates, while all higher states lie outside \mathcal{P}_N and are not algebraically solvable.

B On the convergence of variational calculations

For illustrative purposes, we restrict our attention to the ground-state wavefunction.

For $\lambda = 0$, the exactly solvable (QES) ground state ($n = 0$) is

$$\psi_0(x) = e^{-\frac{1}{4}x^4 - \frac{1}{2}x^2},$$

with the corresponding exact energy

$$E_0 = \frac{1}{2}.$$

Our variational ansatz is constructed to reflect the analytic structure of the exact solution and is written as

$$\psi_0^{(\text{var})}(x; \lambda) = Q_k^{(0)}(x; \lambda) e^{-x^4/4}, \quad (38)$$

where the polynomial prefactor is defined by

$$Q_k^{(0)}(x; \lambda) = \sum_{i=0}^k c_i x^{2i}. \quad (39)$$

This polynomial has degree $2k$ in the coordinate x ; hence, $k = 1$ corresponds to a quadratic approximation, $k = 2$ to a quartic approximation, and so on. Below, in Table 6 we present the relative error ΔE in the ground-state energy as a function of the number of variational parameters employed in the ansatz.

Degree of prefactor $Q_k^{(0)}$	Relative error ΔE	Optimized parameters
2	2.6727×10^{-2}	$a_1 = -0.3126809708$
4	9.7362×10^{-4}	$a_1 = -0.4531994490,$ $a_2 = 0.06722709332$ $a_1 = -0.4912011963,$
6	2.3945×10^{-5}	$a_2 = 0.1080204448,$ $a_3 = -0.01013727919$ $a_1 = -0.4986287422,$
8	4.4247×10^{-7}	$a_2 = 0.12125882396,$ $a_3 = -0.01728711954,$ $a_4 = 0.001160882879$ $a_1 = -0.4998134059,$ $a_2 = 0.12432545252,$
10	6.5691×10^{-9}	$a_3 = -0.01995369865,$ $a_4 = 0.002079244055,$ $a_5 = -0.000107134049$ $a_1 = -0.4999771682,$ $a_2 = 0.12489540008,$
12	8.1665×10^{-11}	$a_3 = -0.02065622957,$ $a_4 = 0.002461369670,$ $a_5 = -0.000200353830,$ $a_6 = 8.287020711 \times 10^{-6}$

Table 6: Relative energy error for the variational ground state at $\lambda = 0$.

The corresponding Shannon entropies in position and momentum space are presented in Table 7.

The Shannon entropy in position space is defined as

$$S_x = - \int_{-\infty}^{\infty} \rho(x) \ln \rho(x) dx, \quad \rho(x) = |\psi(x)|^2. \quad (40)$$

Similarly, the Shannon entropy in momentum space is defined as

$$S_p = - \int_{-\infty}^{\infty} \tilde{\rho}(p) \ln \tilde{\rho}(p) dp, \quad \tilde{\rho}(p) = |\phi(p)|^2, \quad (41)$$

where $\phi(p)$ is the momentum-space wavefunction obtained via the Fourier transform

$$\phi(p) = \frac{1}{\sqrt{2\pi}} \int_{-\infty}^{\infty} \psi(x) e^{-ipx} dx. \quad (42)$$

Degree of $Q_k^{(0)}$	$S_x^{(\text{var})}$	$\frac{ S_x^{(\text{var})} - S_x^{(\text{exact})} }{S_x^{(\text{exact})}}$	$S_p^{(N)}$	$\frac{ S_p^{(\text{var})} - S_p^{(\text{exact})} }{S_p^{(\text{exact})}}$
2	0.8226566228	$3.989180864 \times 10^{-2}$	1.3778410103	$9.809501700 \times 10^{-4}$
4	0.7932084673	$2.667412873 \times 10^{-3}$	1.3795780274	$2.784935788 \times 10^{-4}$
6	0.7911855391	$1.102993113 \times 10^{-4}$	1.3792446341	$3.676299851 \times 10^{-5}$
8	0.7911010621	$3.317926110 \times 10^{-6}$	1.3791985068	$3.317926110 \times 10^{-6}$
10	0.7910983603	$9.955151240 \times 10^{-8}$	1.3791938477	$6.024819014 \times 10^{-8}$
12	0.7910982837	$2.715741793 \times 10^{-9}$	1.3791939566	$1.868646829 \times 10^{-8}$

Table 7: Position-space Shannon entropy S_x and momentum-space Shannon entropy S_p obtained with the variational ansatz of degree $2k$ at $\lambda = 0$ (parameters from Table 6). Exact values: $S_x^{(\text{exact})} = 0.79109828152\dots$ and $S_p^{(\text{exact})} = 1.37919393077\dots$

Now, for $\lambda = 1$ the exact QES ground state ($n = 0$) solution is given by

$$\psi_0 = \left(1 + (\sqrt{3} - 1)x^2\right) e^{-\frac{1}{4}x^4 - \frac{1}{2}x^2},$$

with exact energy

$$E_0 = \frac{3}{2} - \sqrt{3}.$$

In Table 8 we present the relative error ΔE in the ground-state energy as a function of the number of variational parameters employed in the ansatz.

Degree of prefactor $Q_k^{(0)}$	Relative error ΔE	Optimized parameters
2	4.6563×10^{-2}	$a_1 = -0.05860507075$
4	7.6744×10^{-3}	$a_1 = 0.10253495387,$ $a_2 = -0.07314452001$ $a_1 = 0.19677960722,$
6	4.4991×10^{-4}	$a_2 = -0.17203725937,$ $a_3 = 0.02459448236$ $a_1 = 0.22479924945,$
8	1.5361×10^{-5}	$a_2 = -0.22122664714,$ $a_3 = 0.05132969065,$ $a_4 = -0.004372210324$ $a_1 = 0.23082022174,$ $a_2 = -0.23659628008,$
10	3.6657×10^{-7}	$a_3 = 0.06478777917,$ $a_4 = -0.009040695644,$ $a_5 = 0.0005476974990$ $a_1 = 0.23186998035,$ $a_2 = -0.24020220308,$
12	6.7071×10^{-9}	$a_3 = 0.06926098046,$ $a_4 = -0.01148943090,$ $a_5 = 0.001148088913,$ $a_6 = -0.00005358401893$

Table 8: Relative energy error for the variational ground state at $\lambda = 1$.

The associated Shannon entropies in position and momentum space are presented in Table 9.

Degree of $Q_k^{(0)}$	$S_x^{(\text{var})}$	$\frac{ S_x^{(\text{var})} - S_x^{(\text{exact})} }{S_x^{(\text{exact})}}$	$S_p^{(\text{var})}$	$\frac{ S_p^{(\text{var})} - S_p^{(\text{exact})} }{S_p^{(\text{exact})}}$
2	0.9884178551	4.9276×10^{-3}	1.2319666665	2.4055×10^{-2}
4	0.9952220079	1.9127×10^{-3}	1.2594248236	2.3540×10^{-3}
6	0.9935384436	2.1810×10^{-4}	1.2619202139	3.7476×10^{-4}
8	0.9933313443	7.6604×10^{-7}	1.2624182767	1.9855×10^{-5}
10	0.9933218112	2.3122×10^{-7}	1.2623903778	2.2811×10^{-6}
12	0.9933215821	3.1360×10^{-10}	1.2623935474	2.2437×10^{-7}

Table 9: Position-space Shannon entropy S_x and momentum-space Shannon entropy S_p obtained with the variational ansatz of degree $2k$ at $\lambda = 1$ (parameters from Table 8). Exact values: $S_x^{(\text{exact})} = 0.993321580789\dots$ and $S_p^{(\text{exact})} = 1.262393264036\dots$.

Therefore, the convergence of the variational energies mirrors that of the Shannon entropies, indicating that the trial wavefunctions closely reproduce the exact ground state. Since entropies are highly sensitive to the detailed shape of the probability density, their agreement with the exact values confirms the overall accuracy and reliability of the variational approximation.

The present study is focused on the qualitative evolution of phase-space and entropic structures as functions of the control parameter λ , rather than on high-precision benchmarking. All numerical results are stable to at least four significant digits, and further increases in numerical accuracy do not alter the qualitative behavior of the entropy and information-theoretic profiles, nor their visual representation.